

Document downloaded from:

<http://hdl.handle.net/10251/48192>

This paper must be cited as:

Pereira, ALJ.; Gracia, L.; Santamaría-Pérez, D.; Vilaplana Cerda, RI.; Manjón Herrera, FJ.; Errandonea, D.; Nalin, M... (2012). Structural and vibrational study of cubic Sb<sub>2</sub>O<sub>3</sub> under high pressure. *Physical Review B*. 85(17):174108-1-174108-11.  
doi:10.1103/PhysRevB.85.174108.



The final publication is available at

<http://journals.aps.org/prb/pdf/10.1103/PhysRevB.85.174108>

Copyright American Physical Society

# Structural and vibrational study of cubic $\text{Sb}_2\text{O}_3$ under high pressure

A.L.J. Pereira<sup>\*1,2</sup>, L. Gracia<sup>2</sup>, D. Santamaría-Pérez<sup>3</sup>, R. Vilaplana<sup>4</sup>,  
F.J. Manjón<sup>5</sup>, D. Errandonea,<sup>6</sup> M. Nalin,<sup>7</sup> and A. Beltrán<sup>2</sup>

<sup>1</sup>São Paulo State University - UNESP, Advanced Materials Group, Bauru (Brazil)

<sup>2</sup>Departament de Química Física i Analítica, MALTA Consolider Team,  
Universitat Jaume I, 12071 Castelló (Spain)

<sup>3</sup>Departamento de Química Física I, Facultad de Ciencias Químicas,  
Universidad Complutense de Madrid, Madrid (Spain)

<sup>4</sup>Centro de Tecnologías Físicas, MALTA Consolider Team,  
Universitat Politècnica de València, Camí de Vera s/n, 46022 València (Spain)

<sup>5</sup>Instituto de Diseño para la Fabricación y Producción Automatizada, MALTA Consolider Team,  
Universitat Politècnica de València, Camí de Vera s/n, 46022 València (Spain)

<sup>6</sup>Departamento de Física Aplicada-ICMUV, Universidad de Valencia, Edificio de Investigación,  
C/Dr. Moliner 50, 46100 Burjassot, Valencia, Spain.

<sup>7</sup>Departamento de Química, LAVIE, Universidade Federal de São Carlos, São Carlos (Brazil)

## Abstract

We report an experimental and theoretical study of antimony oxide ( $\text{Sb}_2\text{O}_3$ ) in its cubic phase (senarmontite) under high pressure. X-ray diffraction and Raman scattering measurements up to 18 and 25 GPa, respectively, have been complemented with *ab initio* total-energy and lattice dynamics calculations. X-ray diffraction measurements do not provide evidence of a space-group symmetry change in senarmontite up to 18 GPa. However, Raman scattering measurements evidence changes in the pressure coefficients of the Raman mode frequencies at 3.5 and 10 GPa, respectively. The behaviour of the Raman modes with increasing pressure up to 25 GPa is fully reproduced by the lattice-dynamics calculations in cubic  $\text{Sb}_2\text{O}_3$ . Therefore, the combined analysis of both experiments and lattice-dynamics calculations suggest the occurrence of two isostructural phase transformations at 3.5 and 10 GPa, respectively. Total-energy calculations show that the isostructural phase transformations occur through local atomic displacements in which senarmontite losses its molecular character to become a three-dimensional solid. In addition, our calculations provide evidence that cubic senarmontite cannot undergo a phase transition to orthorhombic valentinite at high pressure, and that a phase transition to a  $\beta\text{-Bi}_2\text{O}_3$  type structure is possible above 25 GPa.

**Keywords:** senarmontite, adamantanoid, high pressure, isostructural phase transition

PACS: 62.50.-p, 71.20.Nr, 78.20.Bh, 78.40.Fy

## I. Introduction

Antimony oxide ( $\text{Sb}_2\text{O}_3$ ) is a sesquioxide of late group-15 elements of the Periodic Table, like  $\text{As}_2\text{O}_3$  and  $\text{Bi}_2\text{O}_3$ , with outstanding properties. It is used extensively in industry as a flame retardant in polymers, coatings, and textiles;<sup>1</sup> as a catalyst in the production of polyethylene terephthalate, and polyester resins and fibers;<sup>2</sup> to increase stability and decrease wear of fluid lubricants<sup>3</sup> and in the manufacture of semiconductors and glassy devices.<sup>4-6</sup>

Sesquioxides of late group-15 elements have closely related structures with several polymorphic structures that are not clearly related to those of other sesquioxides, like those of group-13, group 3, and rare earths. In fact, the structures of sesquioxides of late group-15 elements are far from those of simple metal oxides and can be understood on the basis of five array models of the defective fluorite structure. In these sesquioxides, the presence of a lone electron pair in the metal atom plays a central role in determining the local atomic arrangement, as has been recently shown by theoretical calculations.<sup>7</sup>

The solid phases of  $\text{Sb}_2\text{O}_3$  include an amorphous (glassy) and three crystalline structures, senarmontite ( $\alpha\text{-Sb}_2\text{O}_3$ ), valentinite ( $\beta\text{-Sb}_2\text{O}_3$ ), and a very recently found new phase ( $\gamma\text{-Sb}_2\text{O}_3$ ). Senarmontite is a cubic “molecular” crystal composed of spherical-top  $\text{Sb}_4\text{O}_6$  “dimers” that forms an adamantanoid cage with  $T_d$  symmetry and is the predominant form below  $570^\circ\text{C}$ .<sup>5, 8-10</sup> Valentinite has an orthorhombic unit cell, consisting of chains of four-membered rings formed by  $\text{SbO}_3$  pyramids, and is the predominant form above  $570^\circ\text{C}$ .<sup>11</sup> Finally,  $\gamma\text{-Sb}_2\text{O}_3$  is an orthorhombic metastable phase recently obtained after a high-pressure and high-temperature treatment of both senarmontite and valentinite.<sup>12</sup> The structure of senarmontite at ambient pressure is shown in **Figure 1** and it is also found in arsenolite (cubic  $\text{As}_2\text{O}_3$ ) and in  $\delta\text{-Bi}_2\text{O}_3$  (cubic  $\text{Bi}_2\text{O}_3$ ). It can be observed that coordination of Sb is three while

coordination of O is two. The adamantoid structure can be seen as Sb linked to other three Sb by three O atoms in a tetrahedral configuration where one bond is lost due to the presence of a pair of non-bonding electrons in Sb. These adamantoid cages are held together by van der Waals forces to give the molecular solid.

A few high-pressure studies have been reported in sesquioxides of late group-15 for  $\text{As}_2\text{O}_3$ ,<sup>13, 14</sup>  $\text{Bi}_2\text{O}_3$ ,<sup>15, 16</sup> and  $\beta\text{-Sb}_2\text{O}_3$ .<sup>17</sup> These works show that while arsenolite and monoclinic  $\alpha\text{-Bi}_2\text{O}_3$  undergo a crystalline-to-amorphous transition above 15 and 20 GPa, respectively, claudetite (orthorhombic  $\text{As}_2\text{O}_3$ ) remains crystalline to 40 GPa, and a solid-solid phase transition seems to be present near 8 GPa in valentinite. These studies have shown the complex nature of the phase transitions in these sesquioxides and the need to study the pressure-induced phase transitions in other polymorphic phases of these compounds in order to better understand their similarities and differences with respect to other sesquioxides.<sup>18</sup>

In this work, we present a structural and vibrational study of senarmontite up to 25 GPa by means of X-ray diffraction (XRD) and Raman measurements which are complemented with total-energy and lattice-dynamics calculations in the framework of density-functional theory (DFT). We will show that, unlike arsenolite, senarmontite remains in the cubic structure up to 25 GPa and that it suffers two isostructural phase transitions at 3.5 and 10 GPa, respectively, in which senarmontite loses its molecular character to become a three-dimensional solid.

## II. Experimental details

The cubic  $\text{Sb}_2\text{O}_3$  samples used in this work were purchased from Aldrich with grade purity higher than 99% (code 11115). XRD and Raman scattering measurements were performed both at ambient and at high pressures. For both types of high-pressure experiments a mixture of methanol and ethanol with a 4:1 ratio was used as pressure medium and ruby

chips evenly distributed in the pressure chamber were used to measure the pressure by the fluorescence method.<sup>19</sup>

Angle-dispersive XRD measurements on  $\text{Sb}_2\text{O}_3$  were carried out with an Xcalibur diffractometer (Oxford Diffraction Limited). X-ray diffraction patterns were obtained on a 135 mm Atlas CCD detector placed at 110 mm from the sample using  $K_{\alpha 1}$ :  $K_{\alpha 2}$  molybdenum radiation (0.7093 and 0.7136 Å, respectively). The X-ray beam was collimated to a diameter of 300 μm. High-pressure measurements on  $\text{Sb}_2\text{O}_3$  powder were performed in a modified Merrill-Bassett diamond anvil cell (DAC) up to 18 GPa. The diamond anvils used have 500-μm culets. The white  $\text{Sb}_2\text{O}_3$  powder was placed in the 150 μm-diameter holes of the stainless steel gasket pre-indented to a thickness of 50 μm. Exposure times were typically of 1 hour. The diamond cell used for these experiments allows access to an angular range  $4\theta = 50^\circ$ . The observed intensities were integrated as a function of  $2\theta$  in order to give conventional, one-dimensional diffraction profiles. The CrysAlis software, version 171.34.49 (Oxford Diffraction Limited), was used for the data collections and the preliminary reduction of the data. The indexing and refinement of the powder diffraction patterns were performed using the Fullprof<sup>20</sup> and Powdercell<sup>21</sup> program packages. The same procedure was used previously to successfully study the high pressure behaviour of different oxides.<sup>22, 23</sup>

Unpolarized room-temperature Raman scattering experiments in backscattering geometry were performed using a HeNe laser (6328 Å line) with a power below 5 mW in order not to burn the sample. The signal was collected by a Horiba Jobin Yvon LabRAM HR microspectrometer equipped with a TE-cooled multi-channel CCD detector and a spectral resolution better than  $2 \text{ cm}^{-1}$ . High-pressure measurements up to 25 GPa were performed in a membrane-type DAC with diamond anvils having a 400 μm-diameter culet size.

### III. Theoretical Details

DFT calculations were performed with the *CRYSTAL09* program package.<sup>24</sup> Sb and O centers have been described in the scheme of Gaussian basis sets<sup>25</sup> used in other previous works<sup>26</sup> and 6-31G\* respectively. Becke's three-parameter hybrid non local exchange functional<sup>27</sup> combined with the Lee-Yang-Parr gradient-corrected correlation functional, B3LYP,<sup>28</sup> has been used. The standard B3LYP hybrid method has been extensively used for molecules and provides also an accurate description of crystalline structures as bond lengths, binding energies, and band gap values are regarded.<sup>29, 30</sup> The diagonalization of the Fock matrix was performed at adequate  $k$ -points grids in the reciprocal space (Pack-Monkhorst 1976) of shrinking parameters 4–6 depending on the phase being treated (8, 18, 27 and 27  $k$ -points for sernamontite,  $\beta$ -Bi<sub>2</sub>O<sub>3</sub>-type,  $\gamma$ -Sb<sub>2</sub>O<sub>3</sub>, and valentinite-type phases, respectively). The thresholds controlling the accuracy of the calculation of Coulomb and exchange integrals were set to  $10^{-8}$  and  $10^{-14}$  assuring a convergence in total energy better than  $10^{-6}$  a.u. in all cases. The percent of Fock/Kohn-Sham matrix mixing was set to 40.<sup>24</sup> The empirical correction scheme to energy that considers the long-range dispersion contributions proposed by Grimme<sup>31</sup> and implemented by Bücko *et al.*<sup>32</sup> for periodic systems was used in this work. In order to take into account the effect of pressure on this system, we have optimized the geometrical parameters and the internal positions of all phases, at a number of fixed volumes ( $V$ ), where  $V_0$  is the equilibrium unit cell volume. Then, the computed ( $E$ ,  $V$ ) pairs are used to calculate the pressure-volume data by minimizing the enthalpy with respect to  $V$  at selected values of pressure in the range 0-40 GPa. We have also generated values of the zero-pressure bulk modulus and its pressure derivative:  $B_0$  and  $B_0'$ , by means of a numerical fitting procedure consistent with the Birch-Murnaghan<sup>33</sup> EOS. Vibrational-frequency calculations in *CRYSTAL* are performed at the  $\Gamma$  point within the harmonic approximation, and the dynamical

matrix has been computed. The band structures have been obtained along the appropriate high-symmetry paths of the Brillouin zone for the cubic and orthorhombic systems.

## IV. Results and Discussion

### A. XRD and Raman measurements at ambient pressure

At ambient conditions, the crystalline structure of the studied sample was characterized by means of XRD and Raman spectroscopy measurements. **Figure 2** shows the XRD and Raman patterns obtained for  $\text{Sb}_2\text{O}_3$  at ambient pressure. The XRD pattern shows that the phase of  $\text{Sb}_2\text{O}_3$  at ambient pressure is cubic (senarmontite) which belongs to the space group No. 227 ( $Fd\bar{3}m$ ), where the Sb atom occupies a 32e site with  $3m$  symmetry and the O atom occupies a 48f site with  $mm2$  symmetry.<sup>10, 34</sup> The observed diffraction peaks agree very well with the JCPDS data card No. 05-0534. Note that XRD peaks at ambient pressure have been measured within a capillary tube and show larger widths than XRD peaks measured inside the DAC (see **Fig. 3**).

As regards lattice dynamics of  $\text{Sb}_2\text{O}_3$ , there are 2 formula units of  $\text{Sb}_4\text{O}_6$  in the primitive cell and therefore there are 60 normal modes of vibration whose symmetry is:<sup>35</sup>

$$\Gamma_{60} = 2 A_{1g} + 2 A_{1u} + 2 E_u + 2 E_g + 3 F_{2u} + 5 F_{2g} + 5 F_{1u} + 3 F_{1g}$$

where the E modes are doubly degenerated and the F modes are triply degenerated. There are nine Raman-active modes  $\Gamma = 2A_{1g}+2E_g+5F_{2g}$  where one of them is a translational  $F_{2g}$  mode and the rest are internal modes of the adamantoid cage of cubic senarmontite derived from factor group analysis.<sup>13</sup> Raman scattering measurements in  $\text{Sb}_2\text{O}_3$  at ambient pressure show that the most prominent Raman bands are at  $84 \text{ cm}^{-1}$  (translational -  $F_{2g}$ ),  $119 \text{ cm}^{-1}$  ( $E_g$ ),  $190 \text{ cm}^{-1}$  ( $F_{2g}$ ),  $255 \text{ cm}^{-1}$  ( $A_{1g}$ ),  $357 \text{ cm}^{-1}$  ( $F_{2g}$ ),  $374 \text{ cm}^{-1}$  ( $F_{2g}$ ),  $451 \text{ cm}^{-1}$  ( $A_{1g}$ ) and  $715 \text{ cm}^{-1}$  ( $F_{2g}$ ) in agreement with the Raman modes reported to cubic  $\text{Sb}_2\text{O}_3$  senarmontite.<sup>13, 36, 37</sup> A small band at  $141 \text{ cm}^{-1}$  at ambient pressure indicates a residual portion of the valentinite phase. The

positions of these peaks are listed in the **Table 1** for comparison with the results of other works.

## **B. XRD measurements under pressure**

**Figure 3** shows the XRD patterns of  $\text{Sb}_2\text{O}_3$  with increasing pressure up to 18 GPa. The XRD patterns were only collected up to  $18.9^\circ$  because of the presence of the peaks associated to the gasket at higher angles. Four peaks of the cubic senarmontite structure could be measured within this angular range. XRD patterns at different pressures indicate that the cubic symmetry of  $\text{Sb}_2\text{O}_3$  remains unchanged up to the highest pressure attained. It also can be seen that all diffraction peaks markedly shift to larger diffraction angles as pressure increases. The measured lattice constant at ambient conditions is  $a = 11.1466(8) \text{ \AA}$ , which yields a unit-cell volume  $V_0 = 1384.9(3) \text{ \AA}^3$ . The experimental and theoretical pressure dependence of the volume in senarmontite is shown in **Figure 4**. The P–V data are fitted using third-order Birch–Murnaghan<sup>33</sup> EOS to obtain the ambient pressure bulk modulus  $B_0$  and its pressure derivative  $B_0'$ . A good agreement is observed between the theoretical and experimental results reported in **Table 2**. The fit of all data leads to an unusual large value for  $B_0'(13)$ . This large derivative indicates a strong increase in the bulk modulus value of  $\text{Sb}_2\text{O}_3$  as pressure increases. Therefore, taking into account the three pressure ranges obtained by Raman scattering measurements (see next section) it has more physical meaning to fit the P–V data with one EOS for the low-pressure range ( $P < 3.5 \text{ GPa}$ ), another EOS for the intermediate pressure range ( $3.5 \text{ GPa} < P < 10 \text{ GPa}$ ), and another EOS for the high-pressure range ( $P > 10 \text{ GPa}$ ). The results of the EOS obtained in these three ranges are summarized in **Table 2**. Fitting data with three EOS, we achieved more reasonable results for  $B_0'$  with higher bulk modulus for the high-pressure phases above 3.5 and 10 GPa, respectively (see **Table 2**). As we will show later, the three different regions of compressibility are a consequence of the

transformation of  $\text{Sb}_2\text{O}_3$  from a solid with molecular character to a solid with more covalent character.

### C. Raman scattering measurements under pressure

**Figure 5** shows the evolution of the Raman spectra as the sample is subjected to compression. From ambient pressure to 3.5 GPa it can be observed that the  $F_{2g}$  modes, whose frequencies were at 93, 196, 365, 384  $\text{cm}^{-1}$  at ambient pressure, and the  $A_{1g}$  mode at 473  $\text{cm}^{-1}$  shift to higher wavenumbers, while the  $E_g$  (120  $\text{cm}^{-1}$ ),  $A_{1g}$  (263  $\text{cm}^{-1}$ ) and  $F_{2g}$  (709  $\text{cm}^{-1}$ ) modes shift to lower wavenumbers. A change in the pressure coefficients of many vibrational modes without any significant shift in frequency occur at 3.5 GPa. Above this pressure, the new pressure coefficients of the Raman modes remain basically similar till 10 GPa. However, above this pressure, a strong luminescence background appears and four new weak vibrational modes appear (see **Figure 6**). Note that the emerging peaks above 10 GPa are weak and they cannot be observed anymore above 21 GPa. Furthermore, a new change in the pressure coefficients of the Raman modes occurs. The observed changes in the Raman spectra at 3.5 and 10 GPa suggest the occurrence of two phase transitions at these pressures. Finally, top of **Figure 5(b)** shows the Raman spectrum when the pressure is removed after reaching 25 GPa. It has the same pattern as that of the starting material except for broader features, indicating the reversibility of the structural changes suffered by senarmontite in this pressure range.

**Figure 7** shows the experimental Raman frequencies (symbols) as a function of pressure from 0 to 25 GPa. The assignment of the symmetries of the Raman modes, their frequencies and pressure coefficients are presented in **Table 1**. The pressures at which changes in the Raman spectra are observed are marked with dashed vertical lines. As commented, at 3.5 GPa there are considerable changes in the pressure coefficients of the

Raman-active modes. In particular, the  $E_g$  mode ( $120\text{ cm}^{-1}$ ) decreases the pressure dependence from  $-0.71\text{ cm}^{-1}/\text{GPa}$  to  $-0.18\text{ cm}^{-1}/\text{GPa}$  while the modes  $A_{1g}$  ( $263\text{ cm}^{-1}$ ),  $F_{2g}$  ( $365\text{ cm}^{-1}$ ), and  $F_{2g}$  ( $709\text{ cm}^{-1}$ ) change totally the sign of the pressure coefficient. The change of the pressure coefficients of all these vibrational modes indicate that some changes in the Sb-O bonds of the senarmontite structure must be taking place around 3.5 GPa, likely related to the occurrence of a phase transition without any significant change of volume since there is no shift of the Raman mode frequencies at 3.5 GPa. This is in good agreement with the lack of volume change observed by XRD measurements at this pressure. On the other hand, a new change in the pressure coefficients of the Raman modes, without significant shift in frequencies, occurs at 10 GPa. The  $E_g$  mode, initially at  $120\text{ cm}^{-1}$ , changes its pressure coefficient from  $-0.18\text{ cm}^{-1}/\text{GPa}$  to  $0.29\text{ cm}^{-1}/\text{GPa}$ . Likewise, the mode  $F_{2g}$  initially at  $358\text{ cm}^{-1}$  changes from  $-0.71\text{ cm}^{-1}/\text{GPa}$  to  $0.10\text{ cm}^{-1}/\text{GPa}$ . Additionally, the  $E_g$ ,  $A_{1g}$ , and  $F_{2g}$  soft modes, initially at 120, 255, and  $715\text{ cm}^{-1}$ , respectively, that had changed the pressure coefficient at 3.5 GPa, show rather high and positive pressure coefficients above 10 GPa. Finally, the translational mode  $F_{2g}$  ( $93\text{ cm}^{-1}$ ) merge with the mode  $E_g$  around  $115\text{ cm}^{-1}$  near 10 GPa. All the changes at 10 GPa again indicate that a phase transition without a significant change in volume must be occurring at this pressure. Again, our Raman results around 10 GPa are in good agreement with the lack of volume change observed by XRD measurements at this pressure.

**Figure 7(b)** shows the details of the changes of the Raman modes  $A_{1g}$  and  $E_g$  of  $\text{Sb}_2\text{O}_3$  during compression from 0 to 25 GPa. Curiously, the soft  $A_{1g}$  and  $E_g$  modes correspond to symmetric and antisymmetric breathing modes of the  $\text{Sb}_4\text{O}_6$  molecule, respectively. On the other hand, the other soft mode, with  $F_{2g}$  symmetry, can be viewed as a stretching mode of the  $\text{Sb}_4\text{O}_6$  molecule where 2 opposite O and the Sb atoms remain at rest while the other 4 O atoms move enlarging one Sb-O bond and decreasing another Sb-O bond.<sup>36</sup> As it can be

observed clearly, the three  $E_g$ ,  $A_{1g}$ , and  $F_{2g}$  mode frequencies show clearly different pressure coefficients below and above 3.5 and 10 GPa thus suggesting structural changes in the senarmonite structure at those pressures. The pressure dependence of the Raman mode frequencies of these three modes cannot be described by a non-linear function vs. pressure and cannot be simply due to the extraordinary change of the van der Waals forces between the  $Sb_4O_6$  molecules, since there are involved internal modes of the  $Sb_4O_6$  cage where van der Waals forces do not play any role.

In order to check if the changes observed in the Raman mode frequencies correlate with changes in the Raman line widths, we have analyzed the full width at half maximum (FWHM) of several Raman-active modes. **Figure 8** shows the FWHM of the two most intense Raman modes, which are the  $F_{2g}$  and  $A_{1g}$  modes with frequencies near 191 and 255  $cm^{-1}$  at ambient pressure. The peak  $F_{2g}$  shows a slightly increasing FWHM up to 10 GPa and above this pressure there is a sudden increase of the FWHM. Unfortunately, above 16 GPa this peak merges with the  $A_{1g}$  peak and it is difficult to determine the FWHM accurately. On the other hand, the FWHM of the most intense peak ( $A_{1g}$ ) suffers a significant increase till 5 GPa. However, its FWHM decreases quickly above this pressure and remains almost constant till 16 GPa when merges with the  $F_{2g}$  mode. Curiously, both modes have a FWHM that seems to be sensitive only to one of the two structural changes that occur around 3.5 and 10 GPa. Alternatively, another possibility for the broadening with pressure could be a crossing of the frequency of the first order modes with a zone of high density of two phonon states, but it is very strange that the changes occur roughly at the same pressures at which changes in the Raman mode frequencies have been observed.

We think there should be a correlation between the Raman changes observed and the compressibility changes detected around 5 GPa. The changes of the pressure coefficients in the range up to 10 GPa are rather striking since several Raman modes exhibiting rather high

negative pressure coefficients at zero pressure clearly show high positive pressure coefficients above 10 GPa. Another interesting thing is that the merge of phonons that occur above 10 GPa is totally consistent with the fact that the sample becomes more symmetric from 5.2 GPa on, as already commented.

In order to explain the changes in the Raman spectrum and in the compressibility between 3.5 and 10 GPa we have explored theoretically four possible high-pressure phases of senarmontite. In this sense we simulated and compared the structures of valentinite ( $\text{Sb}_2\text{O}_3$  – orthorhombic), claudetite-I and claudetite-II ( $\text{As}_2\text{O}_3$ –monoclinic),<sup>38</sup> and  $\beta\text{-Bi}_2\text{O}_3$  (tetragonal).<sup>39</sup> The results of these calculations show that in the range of pressures used in this work, the cubic  $\text{Sb}_2\text{O}_3$  does not undergo a phase transition to these structures in good agreement with the XRD data. **Figure 9** shows the total energy vs. volume for the senarmontite, valentinite,  $\beta\text{-Bi}_2\text{O}_3$ -like and  $\gamma\text{-Sb}_2\text{O}_3$  phases in  $\text{Sb}_2\text{O}_3$ . Claudetite-I and claudetite-II structures are located at rather high energy values and they are not plotted in **Fig. 9**. An analysis of this figure shows that senarmontite could undergo a phase transition to tetragonal  $\beta\text{-Bi}_2\text{O}_3$ , but only above 25 GPa; i.e., outside our range of pressures of interest. Calculations of the tetragonal structure of  $\beta\text{-Bi}_2\text{O}_3$  provided 34 different vibrational modes that are active in Raman,  $7\text{B}_1+15\text{E}_g+7\text{A}_{1g}+5\text{B}_{1g}$ . Of these modes, 8 vibrational modes have frequencies comparable with those of senarmontite. However, the other 26 Raman modes have not been observed in our Raman spectra up to 25 GPa. Similarly, a very high number of vibrational modes, not observed in our Raman spectra, characterize  $\gamma\text{-Sb}_2\text{O}_3$  phase. Therefore, our calculations give support to the absence of symmetry change in the changes observed in the Raman spectra between 0 and 25 GPa.

Since no high-pressure phase transition is expected in the region between 5 and 10 GPa we tried to understand the pressure behavior of the vibrational modes of senarmontite by performing lattice-dynamics calculations. The theoretical Raman mode frequencies and their

pressure dependences from 0 to 25 GPa are depicted in **Figure 7** (solid lines). They are also summarized in **Table 1**. As can be observed in this figure, the calculated modes of senarmontite are in rather good agreement with the experimental results. Only the Raman-active  $E_g$  mode, theoretically predicted near  $335\text{ cm}^{-1}$ , was not observed experimentally. All pressure dependences of the Raman mode frequencies are well reproduced by calculations with the exception of some modes at low pressures, like the lowest-frequency  $A_{1g}$  mode and the highest-frequency  $F_{2g}$  mode of senarmontite. Curiously, both are soft modes; i.e., they exhibit a negative pressure coefficient. The discrepancy between experimental and calculated pressure coefficients at low pressures can be understood by the molecular character of senarmontite at low pressures and the difficulty of DFT calculations to deal with molecular solids with van der Waals interactions. Note that DFT calculations reproduce well the pressure dependence of all modes above 5 GPa once senarmontite acquires a more covalent character. Due to the relatively good agreement between experimental and theoretical calculations we will now proceed to see if there are structural changes in cubic senarmontite that could help in explaining the changes observed in the compressibility and the vibrational properties of senarmontite at different pressures up to 25 GPa.

#### **D. Structural and electronic changes under pressure**

At ambient pressure the structure of senarmontite is basically composed by molecular units  $Sb_4O_6$  (those that exists in gaseous phase). These units let gaps among themselves and they are weakly bonded (it resembles a structure laminated with strong internal links and weak external links). This can be seen in **Figure 1**, where each Sb atom is bonded to three O atoms and each O atom is bonded to two Sb atoms, being the intramolecular Sb-O bond distances close to  $2\text{ \AA}$  [see squares in **Fig. 10 (a)**]. The tetrahedral arrangement of Sb atoms is completed with the unshared valence electrons (lone pair of electrons). In addition, there are

three O atoms from other molecules whose distance to Sb atoms is approximately 2.9 Å. These intermolecular distances are plotted as circles in **Fig. 10 (a)**.

The nature of bonding and relative bond strengths in the packing arrangement of  $\text{Sb}_4\text{O}_6$  molecules of senarmontite was topologically analyzed by Whitten *et al.* at ambient pressure, verifying the existence of the weak intermolecular bonds.<sup>37</sup> As a result of this type of porous structure, the compound is highly compressible, as confirmed by the small bulk modulus obtained from our XRD measurements. In fact, **Figure 10 (a)** shows that the calculated internal Sb-O bond distances (squares) of the  $\text{Sb}_4\text{O}_6$  molecule are much less compressible than the intermolecular Sb-O distances (circles). These changes in Sb-O bond distances vs. pressure are related to calculated changes in the atomic x coordinate of Sb and O atoms vs. pressure represented in **Fig. 10 (b)**. A rough analysis of **Figures 10 (a) and (b)** could explain the three pressure regimes observed in Raman scattering measurements under pressure. From 0 to 3.5 GPa, the atomic positions vary rapidly with pressure, and the large intermolecular Sb-O distance decreases, while the short intramolecular Sb-O bond distance is almost constant. From 3.5 GPa to 12 GPa the atomic positions tend to increase with a smaller slope, and the large intermolecular Sb-O distance decreases considerably. Also an appreciate decrease of the intramolecular Sb-O bond distance occurs in this pressure range. Finally, above 12 GPa the atomic positions change with a much smaller rate than at lower pressures and the same occurs to the intermolecular Sb-O distance. However, the intramolecular Sb-O distances decrease in a larger rate above 12 GPa. Therefore, our calculations would agree with the existence of two isostructural phase transitions occurring in cubic  $\text{Sb}_2\text{O}_3$  at 3.5 and 12 GPa inferred from the changes observed in the Raman spectrum at 3.5 and 10 GPa. In the following we will show that the above structural changes allow us to explain the observed behavior of senarmontite up to 25 GPa.

There is a large decrease of the intermolecular Sb-O distance up to 3.5 GPa and a rather small decrease of this distance from 12 GPa to 24 GPa. Note that at 12 GPa the intermolecular bond distance is reduced by 7.4%. This means that above this pressure, the intermolecular Sb-O bonds stop being negligible (compared with intramolecular bonds) and consequently there is a smaller change in the atomic positions and the decrease of both Sb-O bond distances is more similar. Thus, our calculations show that the molecular compound tends to become a classic covalent solid above 12 GPa. **Figure 11** shows the senarmontite structure at 20 GPa where Sb atoms are disposed in an octahedral coordination forming distorted  $\text{SbO}_6$  units. The hollow sites almost disappear from the structure and the compound without changing its symmetry is restructured so that it ceases to be a molecular compound resembling a pyrochlore and it acquires a classic covalent solid character composed of  $\text{SbO}_6$  octahedra.

Another interesting feature which supports the isostructural transition taking place in senarmontite is given by the relative intensities of the weak diffraction peaks (111) and (331) with respect of the two most intense peaks (222) and (400). Simulations of XRD patterns with the calculated positions at different pressures show a decrease in intensity of the (111) and (331) peaks with respect to the most intense peaks. This result is in good agreement with the XRD experimental patterns of **Figure 3** where the (111) and (331) peaks have almost disappeared at 17.9 GPa while the (222) and (400) peaks are clearly present.

As regards the extraordinary changes in the Raman spectra, the rather constant value of the calculated intramolecular Sb-O bond distance up to 3.5 GPa would explain the negative pressure coefficients of several modes if we assume that there is a decrease of the strength of some Sb-O bonds. The decrease of some Sb-O bonds can be understood as due to the redistribution of the electronic charges since calculations show that new bonds start being formed on compression above 3.5 GPa. A clear view of the pressure-induced isostructural

transitions taking place in senarmontite can be observed in **Figure 12** where the electronic charge density contours are depicted at 0.0, 9.0 and 24.5 GPa. The contour plots reflect the pass from molecular isolated  $\text{Sb}_4\text{O}_6$  units [**Figure 12 (a)**] to a more compacted structure with  $\text{SbO}_6$  units [**Figure 12 (c)**] in which the O atoms become a bridge between two  $\text{Sb}_4\text{O}_6$  units [**Figures 12 (b)**]. The formation of these new bonds is associated to a reduction of empty sites between molecules. Note the change of coordination of Sb from 3 to 6 and of O from 2 to 4 on increasing pressure (see **Figures 1 and 11**).

As regards Raman changes above 3.5 GPa, we have measured slightly increasing values of the Raman frequencies between 3.5 GPa and 10 GPa and much larger positive pressure coefficients above 10 GPa. These behaviors can be explained by the small reduction of the calculated intramolecular Sb-O distances between 3.5 and 12 GPa, and the larger reduction of the calculated intramolecular Sb-O bond distances above 12 GPa. Therefore, our Raman measurements and calculations point out the existence of two isostructural phase transitions near 3.5 and 10-12 GPa.

To reinforce the idea that two pressure-induced isostructural transitions occur in senarmontite, we have calculated the normalized enthalpy at different pressures for three isostructural phases. The difference between each phase is the evolution of atomic positions which are forced to follow in the whole pressure range the pressure evolution found for each of the three different pressure ranges that we report in **Figure 10**: 0-3.5 GPa (Phase I), 3.5-11 GPa (Phase II), 11-25 GPa (Phase III). The obtained results are shown in **Figure 13**, where it can be seen the I-II-III structural sequence confirming that senarmontite undergoes two isostructural phase transitions up to 25 GPa.

For the sake of completeness, we want to make some comments on the electronic band structure of senarmontite and its electronic density of states projected on atoms and orbitals at different pressures. Our results point out that for all the three pressure ranges studied the

valence- and conduction-band edges are dominated by O  $2p$  and Sb  $5p$  states, respectively, although significant changes in atomic contributions can be pointed out with increasing pressure. The density of states projected on atoms and orbitals for senarmontite at ambient pressure and at 20 GPa is depicted in **Figures 14 (a) and (b)**, respectively. An analysis of this figure shows that the pressure-induced isostructural transitions can be related to changes in hybridization between Sb  $5s$  and O  $2p$  electrons. The two Sb  $5s$  electrons remaining in the valence-band, which forms the adamantanoid molecule, promote to  $p$  levels with pressure. This occupation of  $p$  levels of Sb favors the hybridization between Sb  $5s$  and O  $2p$  electrons to generate the covalent compound. At ambient pressure the valence-band maximum is mainly composed by O  $2p$  states with a minor contribution of Sb  $5s$  states [see **Figure 14 (a)**] while at 20 GPa [see **Figure 14 (b)**] both states contribute evenly to the topmost valence bands in the vicinity of Fermi energy. Regarding to the lowermost conduction band, the contribution of Sb  $5s$  ( $5p$ ) states increases (decreases) with increasing pressure. This is in agreement with the electronic charge density maps of **Figure 12**. On the other hand, the value of the indirect ( $L-\Gamma$ ) bandgap energy is 4.7 eV at ambient pressure and decreases in a continuous way with pressure acquiring the system a more semiconductor character with a bandgap energy of 3.9 eV at 15 GPa.

Finally, we want to mention that pressure-induced isostructural phase transformations are relatively exotic phenomena, in many cases related to a change in the electronic structure. They have been reported for a few elements, like Ce (a well-known example of the isostructural transition),<sup>40</sup> Zr,<sup>41</sup> Os,<sup>42</sup> and recently B.<sup>43</sup> In some cases, the isostructural phase transition is related to compounds containing elements with a variable chemical valence due to fully or partially free  $d$ - or/and  $f$ -electronic shells (for example, SmS,<sup>44</sup> EuCo<sub>2</sub>P<sub>2</sub>,<sup>45</sup> rare-earth chalcogenides<sup>46</sup> and pnictides,<sup>47</sup> or/and materials which undergo magnetic or spin transitions, e.g., MnO<sup>48</sup> or YCo<sub>5</sub>.<sup>49</sup> Finally, we could mention the case of the topological

insulators  $\text{Bi}_2\text{Te}_3$ ,<sup>50, 51</sup>  $\text{Bi}_2\text{Se}_3$ ,<sup>52</sup> and  $\text{Sb}_2\text{Te}_3$ ,<sup>53-55</sup> where a pressure-induced isostructural phase transition seems to be related to an electronic topological transition (ETT) driven by the distortion of the electronic band structure near the Fermi surface resulting in a topological van Hove singularity crossing the Fermi level. Similarly, recent theoretical calculations predict a first-order isostructural transformation in  $\text{PdN}_2$  driven by a phase transition of the electronic structure, which is manifested by a discontinuous change in the hybridization between Pd d and N p electrons as well as a conversion from single to triple bonded nitrogen dimmers.<sup>56</sup> It is noteworthy that senarumontite undergoes two consecutive isostructural phase transitions. Furthermore, it is strange that arsenolite ( $\alpha\text{-As}_2\text{O}_3$ ), having the same structure of senarumontite, do not undergo similar pressure-induced phase transitions. As already commented, arsenolite has been recently studied and a solid-to-amorphous phase transition has been observed near 15 GPa, followed by an amorphous-to-amorphous phase transition near 25 GPa. In fact, no anomaly in the behavior of the Raman modes was observed.<sup>14</sup> The other compound isostructural to senarumontite is  $\delta\text{-Bi}_2\text{O}_3$  whose behavior under pressure is still unknown. However, Jovalekic *et al.*<sup>55</sup> compared the Bi-O bond distances in the  $\text{BiO}_6$  polyhedra for different structural  $\text{Bi}_2\text{O}_3$  phases. The increase in coordination when going from  $\delta\text{-Bi}_2\text{O}_3$  to  $\beta\text{-Bi}_2\text{O}_3$  is in good agreement with our calculations which point to an increase in coordination if cubic  $\text{Sb}_2\text{O}_3$  undergoes a phase transition to the  $\beta\text{-Bi}_2\text{O}_3$  structure. In this sense, we can consider that the two isostructural phase transitions without symmetry change indeed prepare the  $\text{SbO}_6$  arrangement to achieve the tetragonal  $\beta\text{-Bi}_2\text{O}_3$ -type structure above 20 GPa.

## V. Conclusions

In this work we present a structural and vibrational study of senarmontite up to 25 GPa by means of XRD and Raman measurements which are complemented with DFT-based total-energy and lattice-dynamics *ab initio* calculations. We have observed striking changes of the pressure coefficients of the Raman-active modes around 3.5 and 10 GPa. However, XRD measurements evidence no change in the cubic symmetry of the compound up to 18 GPa but just a significant change in compressibility with increasing pressure, without a change in volume. All these features have been understood thanks to theoretical calculations which show that senarmontite remains in the cubic structure up to 20 GPa and undergoes two isostructural phase transitions that lead senarmontite from a low-density phase to a high-density phase above 10-12 GPa. In the isostructural phase transitions senarmontite loses its molecular character, with van der Waals interactions between the adamantoid  $\text{Sb}_4\text{O}_6$  molecules, to become a three-dimensional covalent solid. This transformation is related to changes in hybridization between Sb 5s and O 2p electrons resulting in considerable changes of the mechanical, vibrational, and electronic properties. Furthermore, our calculations suggest that senarmontite does not undergo a pressure-induced phase transition at room temperature neither to valentinite, nor to the monoclinic structures of  $\text{As}_2\text{O}_3$  (claudetite-I and claudetite-II), nor to the recently found  $\gamma\text{-Sb}_2\text{O}_3$  phase, but it could undergo a phase transition to tetragonal  $\beta\text{-Bi}_2\text{O}_3$  above 25 GPa despite Raman measurements have shown no evidence for this transition up to 25 GPa.

## **Acknowledgments**

Financial support from the Spanish Consolider Ingenio 2010 Program (Project No. CDS2007-00045) is acknowledged. The work was also supported by Spanish MICCIN under Project No. CTQ2009-14596-C02-01 and MAT2010-21270-C04-01/04 as well as from

Comunidad de Madrid and European Social Fund: S2009/PPQ-1551 4161893 (QUIMAPRES) and from Vicerrectorado de Investigación de la Universitat Politècnica de València under projects UPV2011-0914 PAID-05-11 and UPV2011-0966 PAID-06-11. It is also acknowledged Spanish Fundació Bancaixa project nº P1-1A2009-08 and Brazilian Capes/Fundación Carolina (BEX 3939/10-3).

## References

1. S. Boryniec and W. Przygocki, *Prog. Rub. Plast. Tech.* **17**, 59 (2001).
2. J. H. Youk, R. P. Kambour and W. J. MacKnight, *Macromolec.* **33**, 3594 (2000).
3. J. S. Zabinski, M. S. Donley and N. T. McDevitt, *Wear* **165**, 103 (1993).
4. A. Ghosh and D. Chakravorty, *J. Phys.: Condens. Matter* **3**, 3335 (1991).
5. P. S. Gopalakrishnan and H. Manohar, *J. Solid State Chem.* **15**, 61 (1975).
6. W. H. Zachariasen, *J. Am. Chem. Soc.* **54**, 3841-3851 (1932).
7. A. Matsumoto, Y. Koyama, A. Togo, M. Choi and I. Tanaka, *Phys. Rev. B* **83**, 214110 (2011).
8. P. J. Miller and C. A. Cody, *Spectrochim. Acta Part a* **38**, 555 (1982).
9. C. Svensson, *Acta Crystallogr. Sect. B: Struct. Sci.* **31**, 2016 (1975).
10. C. Wood, B. Vanpelt and A. Dwight, *Physica Status Solidi B* **54**, 701 (1972).
11. M. Nalin, Y. Messaddeq, S. J. L. Ribeiro, M. Poulain, V. Briois, G. Brunklus, C. Rosenhalm, B. D. Mosel and H. Eckert, *J. Mater. Chem.* **14**, 3398 (2004).
12. D. Orosel, R. E. Dinnebier, V. A. Blatov and M. Jansen, *Struct. Sci.: Sect. B* **68**, 1 (2012).
13. A. Grzechnik, *J. Solid State Chem.* **144**, 416 (1999).

14. E. Soignard, S. A. Amin, Q. Mei, C. J. Benmore and J. L. Yarger, *Phys. Rev. B* **77**, 144113 (2008).
15. C. Chouinard and S. Desgreniers, *Solid State Commun.* **113**, 125 (1999).
16. S. A. Ghedia, Universität Stuttgart, 2010.
17. A. Geng, L. Cao, C. Wan and Y. Ma, *Phys Status Solidi C* **8**, 1708 (2011).
18. F. J. Manjon and D. Errandonea, *Physica Status Solidi B* **246**, 9 (2009).
19. H. K. Mao, J. Xu and P. M. Bell, *J. Geophys. Res.* **91**, 4673 (1986).
20. J. Rodríguez-Carvajal, *Physica B* **192**, 55 (1993).
21. G. Nolze and W. Kraus, *Powder Diffraction* **13**, 256 (1998).
22. D. Errandonea, D. Santamaria-Perez, T. Bondarenko and O. Khyzhun, *Mater. Res. Bull.* **45**, 1732 (2010).
23. D. Errandonea, D. Santamaria-Perez, S. N. Achary, A. K. Tyagi, P. Gall and P. Gougeon, *J. Appl. Phys.* **109**, 043510 (2011).
24. R. Dovesi, V. R. Saunders, C. Roetti, R. Orlando, C. M. Zicovich-Wilson, F. Pascale, B. Civalleri, K. Doll, N. M. Harrison, I. J. Bush, P. D'Arco and M. Llunell, CRYSTAL09 program (2009).
25. [http://www.tcm.phy.cam.ac.uk/~mdt26/basis\\_sets/Sb\\_basis.txt](http://www.tcm.phy.cam.ac.uk/~mdt26/basis_sets/Sb_basis.txt).
26. D. G. Stroppa, L. A. Montoro, A. Beltran, T. G. Conti, R. O. da Silva, J. Andres, E. Longo, E. R. Leite and A. J. Ramirez, *J. Am. Chem. Soc.* **131**, 14544 (2009).
27. A. D. Becke, *J. Chem. Phys.* **98**, 5648 (1993).
28. C. T. Lee, W. T. Yang and R. G. Parr, *Phys. Rev. B* **37**, 785 (1988).
29. C.-H. Hu and D. P. Chong, *Encyclopedia of Computational Chemistry*. (Wiley, Chichester, 1998).
30. L. Gracia, A. Beltran and J. Andres, *J. Phys. Chem. B* **110**, 23417 (2006).
31. S. Grimme, *J. Comput. Chem.* **27**, 1787 (2006).

32. T. Bucko, J. Hafner, S. Lebegue and J. G. Angyan, *J. Phys. Chem. A* **114**, 11814 (2010).
33. F. Birch, *J. Geophys. Res.* **57**, 227 (1952).
34. A. E. Whitten, B. Dittrich, M. A. Spackman, P. Turner and T. C. Brown, *Dalton Trans.*, 23-29 (2004).
35. E. Kroumova, M. I. Aroyo, J. M. Perez-Mato, A. Kirov, C. Capillas, S. Ivantchev and H. Wondratschek, *Phase Transitions* **76**, 155 (2003).
36. C. A. Cody, L. Dicarlo and R. K. Darlington, *Inorg. Chem.* **18**, 1572 (1979).
37. S. J. Gilliam, J. O. Jensen, A. Banerjee, D. Zeroka, S. J. Kirkby and C. N. Merrow, *Spectrochim. Acta Part a* **60**, 425 (2004).
38. G. Mestl, P. Ruiz, B. Delmon and H. Knozinger, *J. Phys. Chem.* **98**, 11276 (1994).
39. S. K. Blower and C. Greaves, *Acta Crystallogr. Sect C: Crystal Struct. Commun.* **44**, 587 (1988).
40. B. Johansson and S. Li, *Philosophical Magazine* **89**, 1793 (2009).
41. Y. Akahama, M. Kobayashi and H. Kawamura, *J. Phys. Soc. Jap.* **60**, 3211 (1991).
42. F. Occelli, D. L. Farber, J. Badro, C. M. Aracne, D. M. Teter, M. Hanfland, B. Canny and B. Couzinet, *Phys. Rev. Lett.* **93**, 095502 (2004).
43. E. Zarechnaya, N. Dubrovinskaia, R. Caracas, M. Merlini, M. Hanfland, Y. Filinchuk, D. Chernyshov, V. Dmitriev and L. Dubrovinsky, *Phys. Rev. B* **82**, 184111 (2010).
44. A. Chatterj and A. K. Singh, *Phys. Rev. B* **6**, 2285 (1972).
45. M. Chefki, M. M. Abd-Elmeguid, H. Micklitz, C. Huhnt, W. Schlabit, M. Reehuis and W. Jeitschko, *Phys. Rev. Lett.* **80**, 802 (1998).
46. R. Caracas and X. Gonze, *Phys. Rev. B* **69**, 144114 (2004).
47. A. Svane, P. Strange, W. M. Temmerman, Z. Szotek, H. Winter and L. Petit, *Physica Status Solidi B* **223**, 105 (2001).

48. C. S. Yoo, B. Maddox, J. H. P. Klepeis, V. Iota, W. Evans, A. McMahan, M. Y. Hu, P. Chow, M. Somayazulu, D. Hausermann, R. T. Scalettar and W. E. Pickett, *Phys. Rev. Lett.* **94**, 115502 (2005).
49. H. Rosner, D. Koudela, U. Schwarz, A. Handstein, M. Hanfland, I. Opahle, K. Koepf, M. D. Kuz'min, K. H. Müller, J. A. Mydosh and M. Richter, *Nature Phys.* **2**, 469 (2006).
50. A. Polian, M. Gauthier, S. M. Souza, D. M. Triches, J. C. de Lima and T. A. Grandi, *Phys. Rev. B* **83**, 113106 (2011).
51. R. Vilaplana, O. Gomis, F. J. Manjon, A. Segura, E. Perez-Gonzalez, P. Rodriguez-Hernandez, A. Munoz, J. Gonzalez, V. Marin-Borras, V. Munoz-Sanjose, C. Drasar and V. Kucek, *Phys. Rev. B* **84**, 104112 (2011).
52. R. Vilaplana, D. Santamaría-Pérez, O. Gomis, F. J. Manjón, J. González, A. Segura, A. Muñoz, P. Rodríguez-Hernández, E. Pérez-González, V. Marín-Borrás, V. Muñoz-Sanjose, C. Drasar and V. Kucek, *Phys. Rev. B* **84**, 184110 (2011).
53. N. Sakai, T. Kajiwara, K. Takemura, S. Minomura and Y. Fujii, *Solid State Commun.* **40**, 1045 (1981).
54. M. K. Jacobsen, R. S. Kumar, A. L. Cornelius, S. V. Sinogeiken and M. F. Nicol, in *Shock Compression of Condensed Matter - 2007, Pts 1 and 2*, edited by M. Elert, M. D. Furnish, R. Chau, N. C. Holmes and J. Nguyen (2007), Vol. 955, pp. 171-174.
55. S. M. d. Souza, D. M. Trichês, C. M. Poffo, J. C. d. Lima, T. A. Grandi and R. S. Biasi, *J. Appl. Phys.* **109**, 013512 (2011).
56. D. Aberg, P. Erhart, J. Crowhurst, J. M. Zaug, A. F. Goncharov and B. Sadigh, *Phys. Rev. B* **82**, 104116 (2010).

**Table 1.** Zero-pressure Raman frequencies and pressure coefficients in different pressure ranges in senarmontite.

Symmetry	Calculated Frequency (cm <sup>-1</sup> )	Experimental Frequency (cm <sup>-1</sup> )		Theoretical $\frac{\partial \nu}{\partial P}$ (cm <sup>-1</sup> /GPa)			Experimental $\frac{\partial \nu}{\partial P}$ (cm <sup>-1</sup> /GPa)			Assignment
		This Work	Mestl et al. [38]	0-5GPa	5-10GPa	10-25GPa	0-5GPa	5-10GPa	10-25GPa	
F <sub>2g</sub>	93	85	82	3.54	1.78	0.37	3.81	-	0.48	Translational Mode
E <sub>g</sub>	121	120	118	-0.50	0.06	0.44	-0.71	-0.18	0.29	Sb-O-Sb bend
F <sub>2g</sub>	196	191	189	3.14	3.14	3.14	3.18	3.18	3.18	Sb-O-Sb bend
A <sub>g</sub>	263	255	254	0.46	0.82	1.53	-1.30	0.39	1.03	Sb-O-Sb stretch
E <sub>g</sub>	335	-	-	-2.46	-2.46	0.83	-	-	-	Sb-O-Sb stretch
F <sub>2g</sub>	365	358	355	-0.23	-0.76	0.58	2.27	-0.71	0.10	Sb-O-Sb stretch
F <sub>2g</sub>	384	374	373	4.25	4.25	4.25	4.57	4.57	4.57	Sb-O-Sb stretch
A <sub>g</sub>	473	452	450	2.49	2.49	2.49	2.59	2.59	2.59	Sb-O-Sb bend
F <sub>2g</sub>	709	715	712	2.07	1.50	2.75	-3.14	0.94	2.13	Sb-O-Sb stretch

**Table 2.** E-V data fitted with three EOS, one for the data covering all the range from 0 to 18 GPa (all range), one for values with  $P < 3.5$  GPa (range 1), another for  $3.5 \text{ GPa} < P < 10$  GPa (range 2) and another for  $P > 10$  GPa (range 3)

	$V_0$ ( $\text{\AA}^3$ )	$B_0$ (GPa)	$B_0'$
Exp. (all range)	1386(5)	16.5(2)	13.4(1)
Theory (all range)	1420(4)	28(3)	12.4(1)
Exp. (range 1)	1380(4)	20(2)	9.4(2)
Theory (range 1)	1443(4)	21(3)	6.0(1)
Exp. (range 2)	1362(8)	25(2)	9.4(3)
Theory (range 2)	1416(9)	36(4)	7.1(1)
Exp. (range 3)	1351(6)	27(1)	9.4(3)
Theory (range 3)	1389(9)	47(4)	8.0(1)

## Figures caption

**Figure 1.** (Color online) Structure of senarmontite at ambient pressure. Sb atoms are big blue balls while O atoms are small red balls. It is composed of molecular  $\text{Sb}_4\text{O}_6$  units (see darker atoms and bond) linked by van der Waals forces. Note that Sb and O have three-fold and two-fold coordination, respectively.

**Figure 2.** a) X-ray diffraction and (b) Raman scattering pattern of the  $\text{Sb}_2\text{O}_3$  powder measured at ambient conditions. Note that XRD peaks at ambient pressure have been measured within a capillary tube and show larger widths than XRD peaks measured inside the DAC.

**Figure 3.** Room-temperature x-ray diffraction patterns of senarmontite measured at different pressures.

**Figure 4.** Equation of state for  $\text{Sb}_2\text{O}_3$  senarmontite. The open circles represent the theoretical data and the solid circles the experimental results. The lines overlaid on the circles are the Birch–Murnaghan equation of state fit of the data.

**Figure 5.** Room-temperature Raman spectra of  $\text{Sb}_2\text{O}_3$  at different pressures: a) ambient to 8 GPa; b) 10 to 25 GPa. In a) triangles and marks indicate the experimental and theoretical (DFT) position of the Raman-active modes at ambient pressure, respectively. In b) the top Raman spectrum is the measurement at atmospheric pressure after decompression from 25 GPa.

**Figure 6.** Detail of Raman spectra above 10 GPa showing the new peaks that appear above this pressure.

**Figure 7.** (Color online) (a) Pressure dependence of Raman modes of  $\text{Sb}_2\text{O}_3$  during compression from 0 to 25 GPa. Symbols represent the experimental data and lines the calculation results. Open symbols represent new Raman bands which appear above 10 GPa. (b) Detailed pressure dependence of the  $A_g$  and  $E_g$  of  $\text{Sb}_2\text{O}_3$  during compression

from 0 to 25 GPa. Symbols represent the experimental data and the solid lines indicate the three different pressure coefficients of these two modes up to 25GPa.

**Figure 8.** (Color online) Full width at half maximum (FWHM) of the most intense  $F_{2g}$  and  $A_g$  modes as a function of pressure.

**Figure 9.** Total energy as a function of volume for the senarmontite, valentinite,  $\beta$ - $Bi_2O_3$ -like and  $\gamma$ - $Sb_2O_3$  phases in  $Sb_2O_3$ . Claudetite-I and claudetite-II forms are located at high energy values.

**Figure 10.** (a) Calculated internal (squares) and external (circles) Sb-O distances of the  $Sb_4O_6$  cage as a function of pressure. (b) Calculated atomic coordinate x of Sb (squares) and x of O (circles).

**Figure 11.** (Color online) Structure of senarmontite at 15 GPa. Sb atoms are big blue balls while O atoms are small red balls. It is composed of  $SbO_6$  octahedra where Sb and O have 6 and 4 coordination, respectively.

**Figure 12.** Total charge density projected on the plane containing three Sb bridge atoms bonded to three O of  $Sb_4O_6$  units, a) at 0.0 GPa , b) at 9.0 GPa and c) at 24.5 GPa.

**Figure 13.** Different linear behavior of enthalpy variation in senarmontite at some ranges of pressures, according to DFT calculations.

**Figure 14.** Density of states projected on atoms and orbitals for senarmontite (a) at ambient pressure and (b) at 20 GPa.

**Fig. 1**

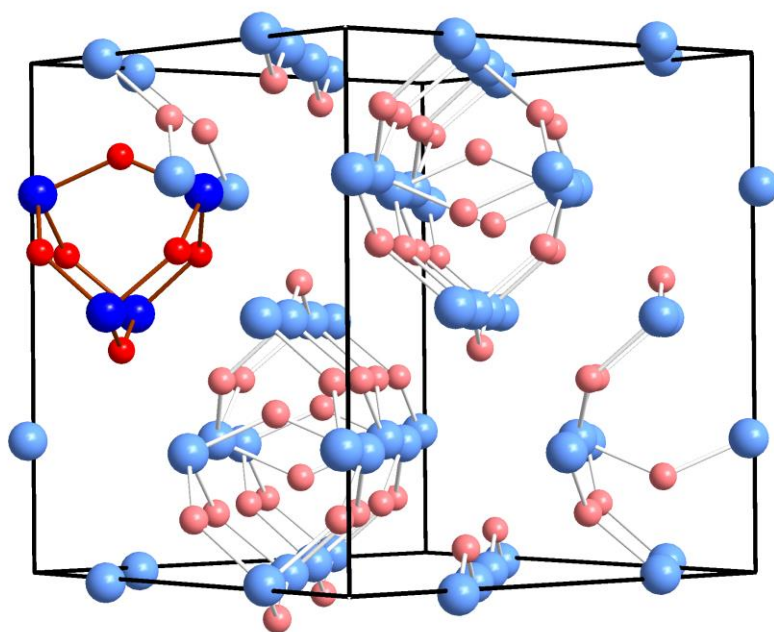
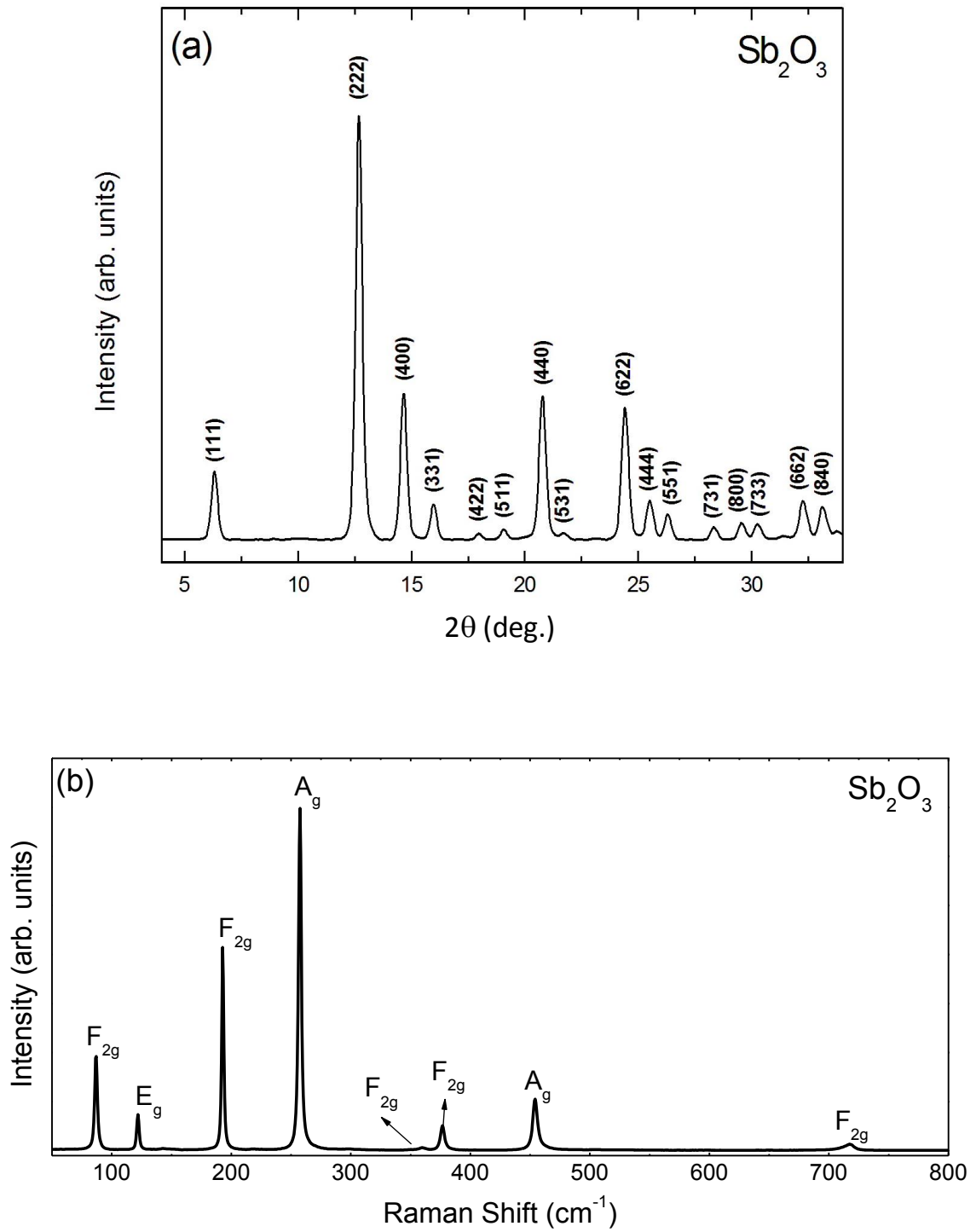
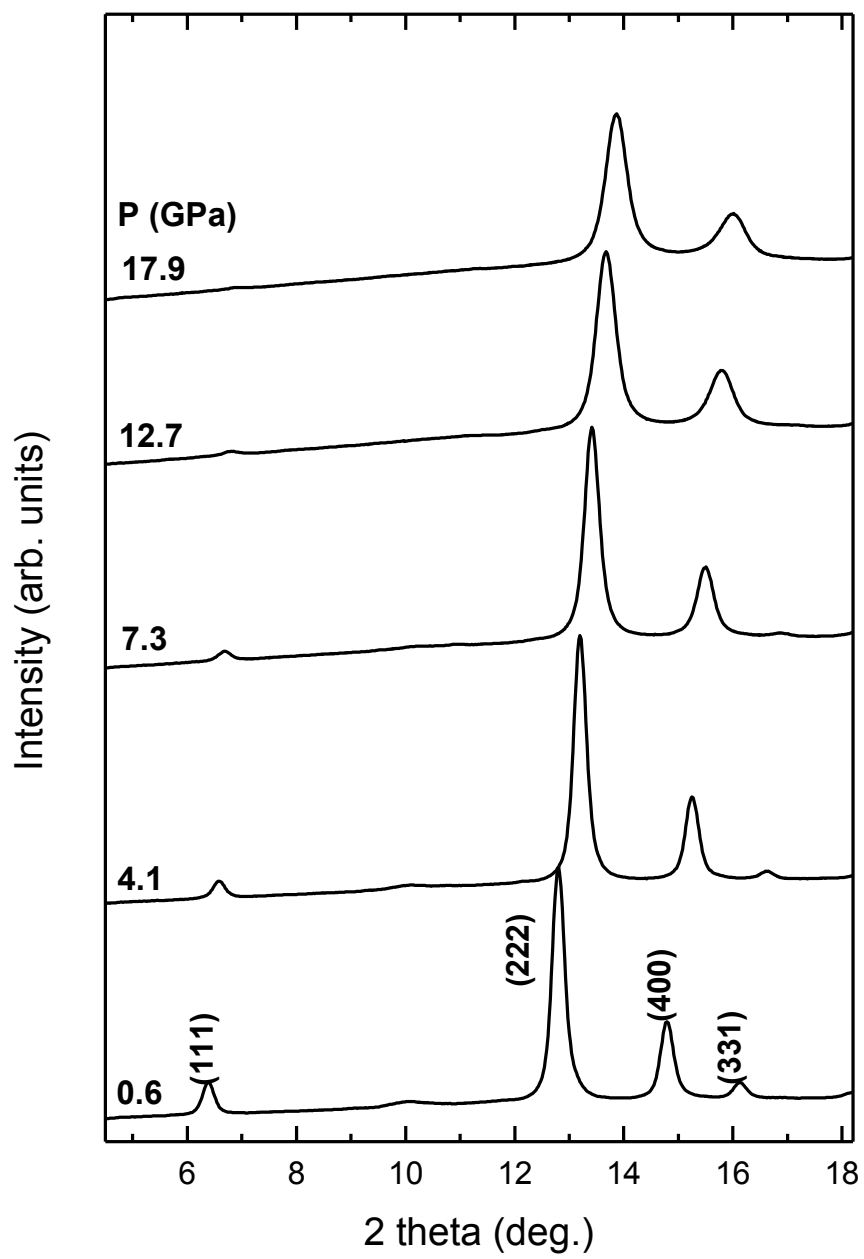


Fig. 2



**Fig. 3**



**Fig. 4**

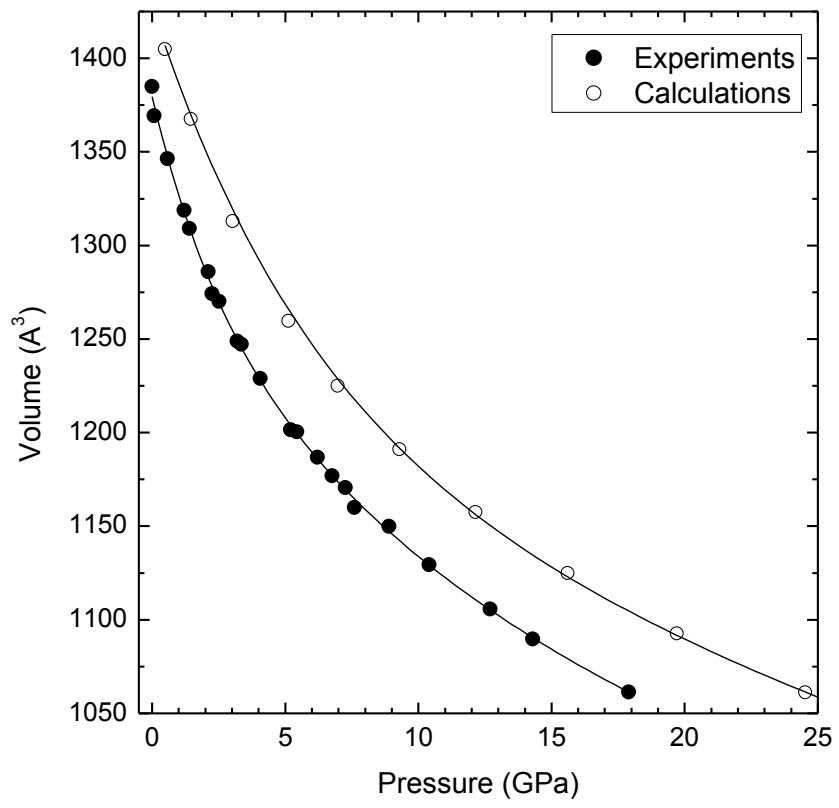


Fig. 5

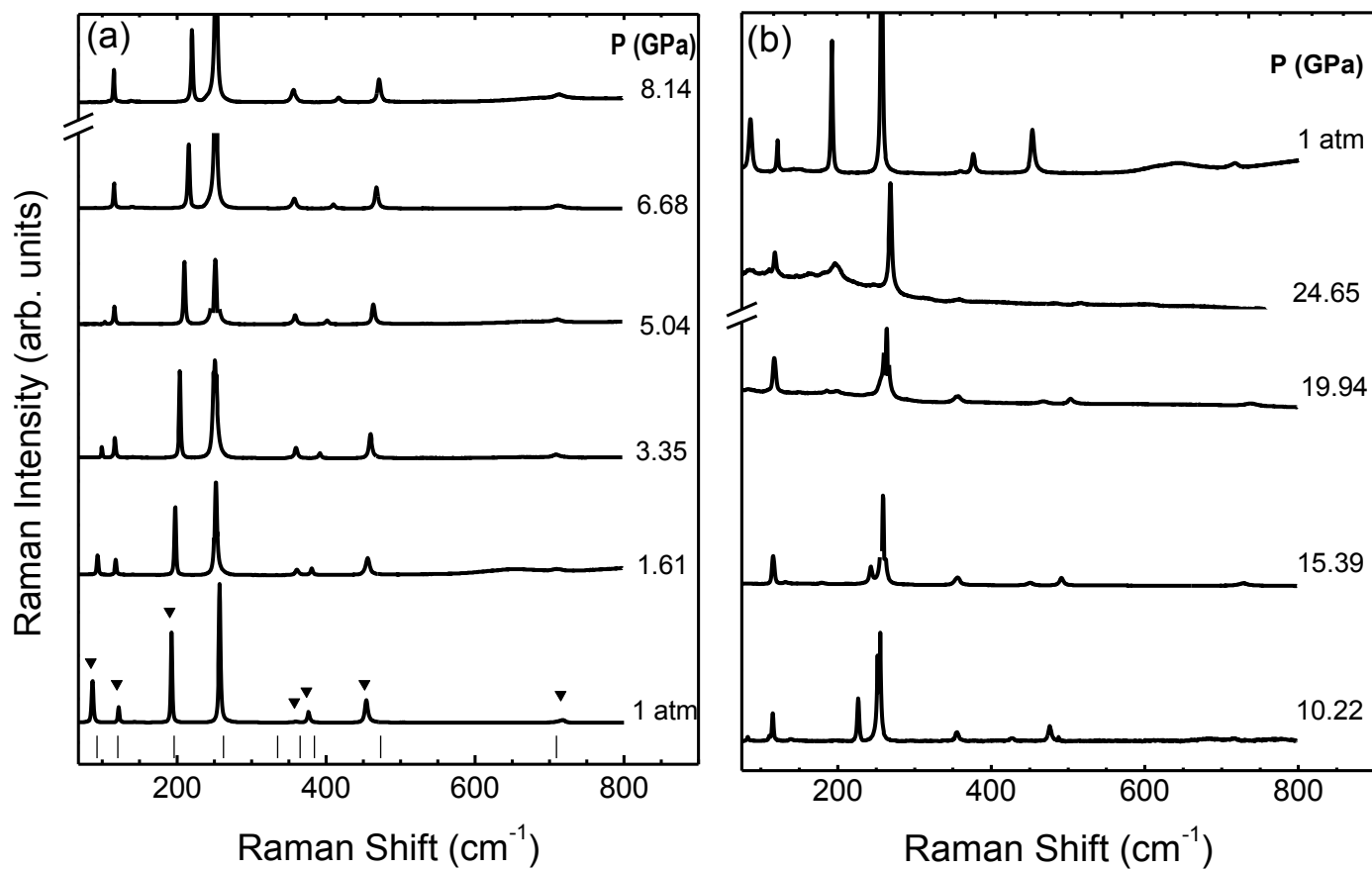


Fig. 6

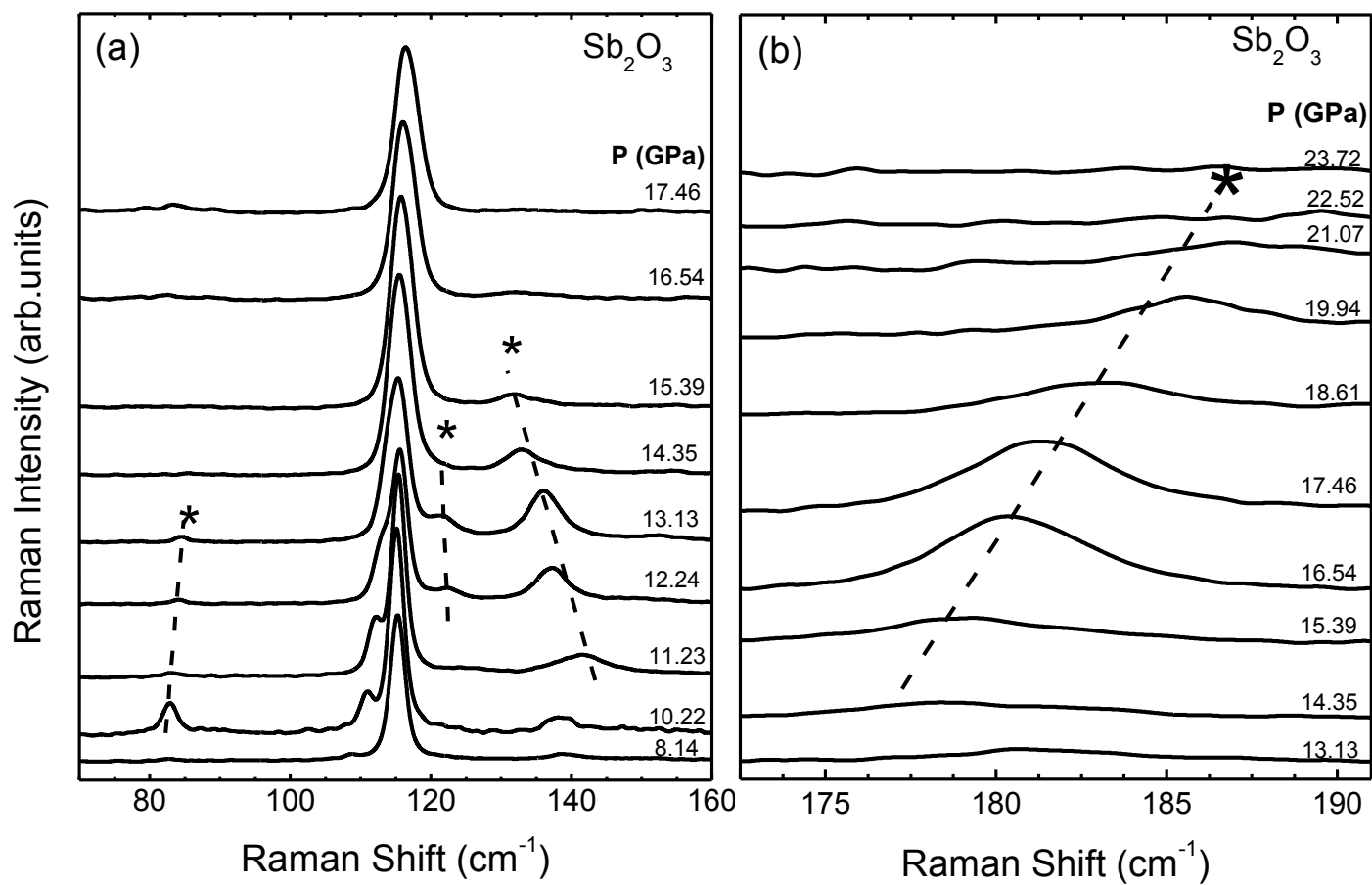
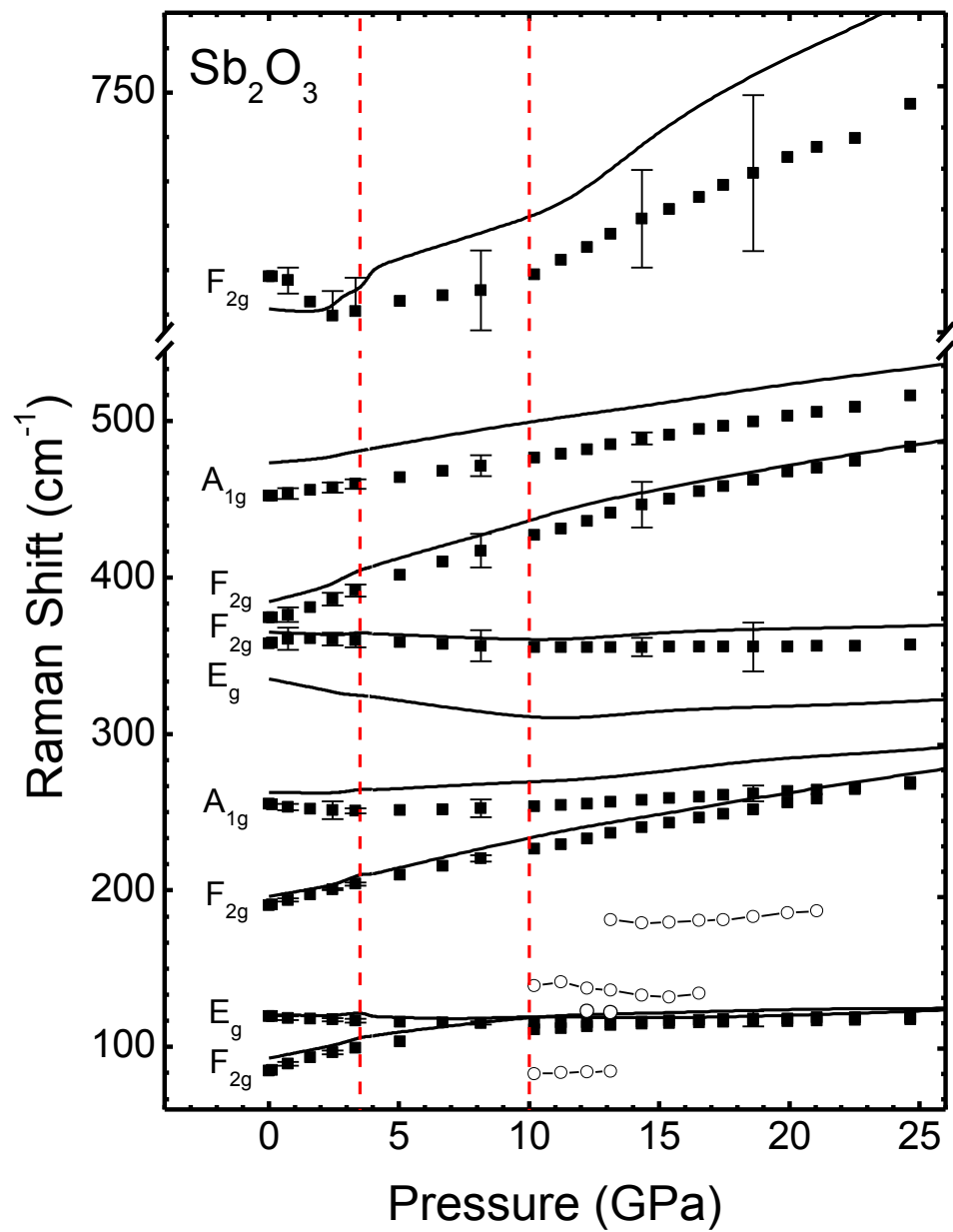


Fig. 7(a)



**Fig. 7(b)**

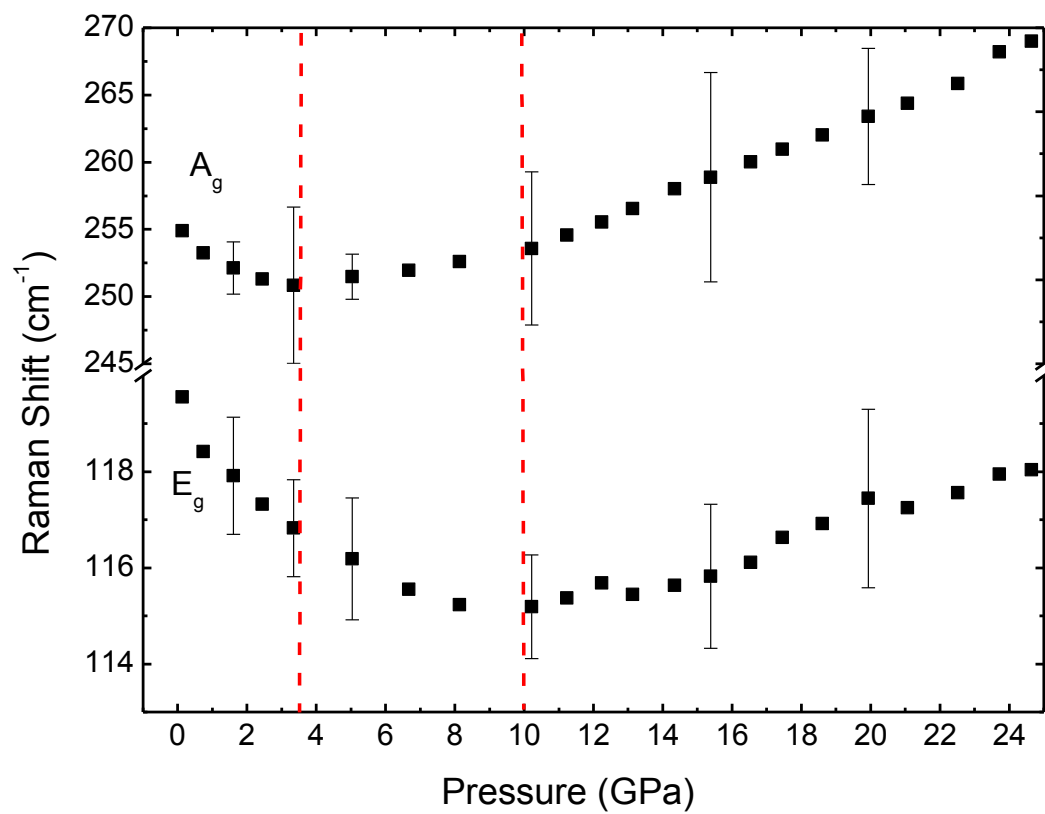


Fig. 8

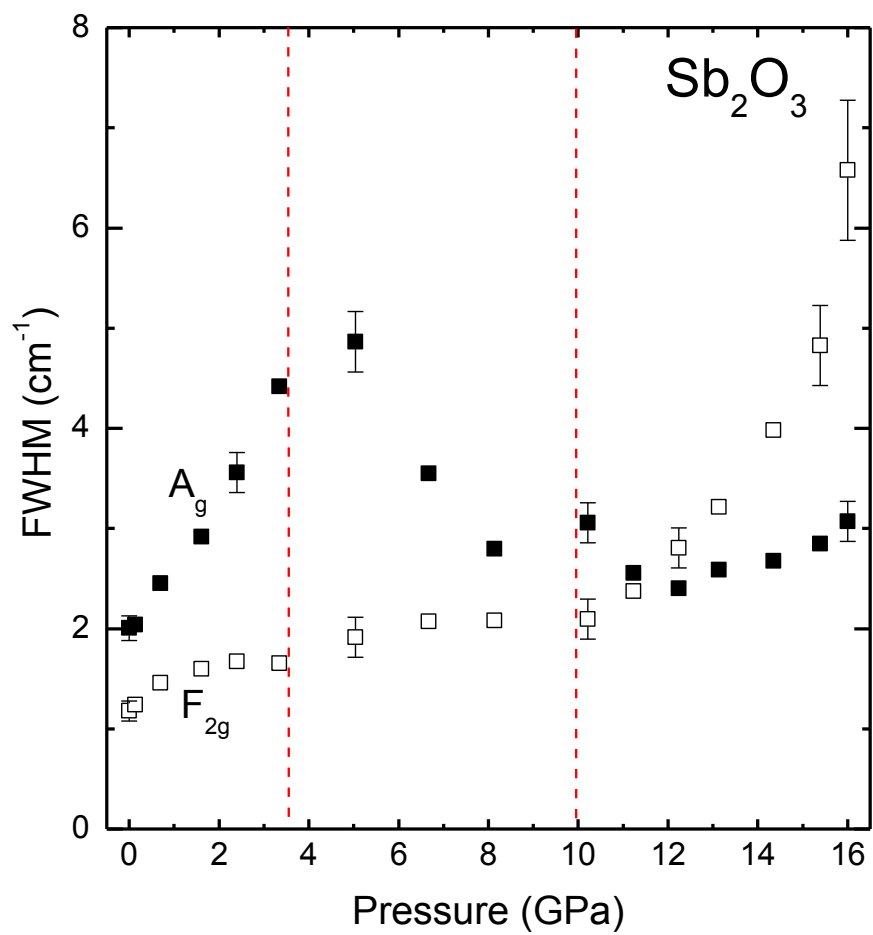


Fig. 9

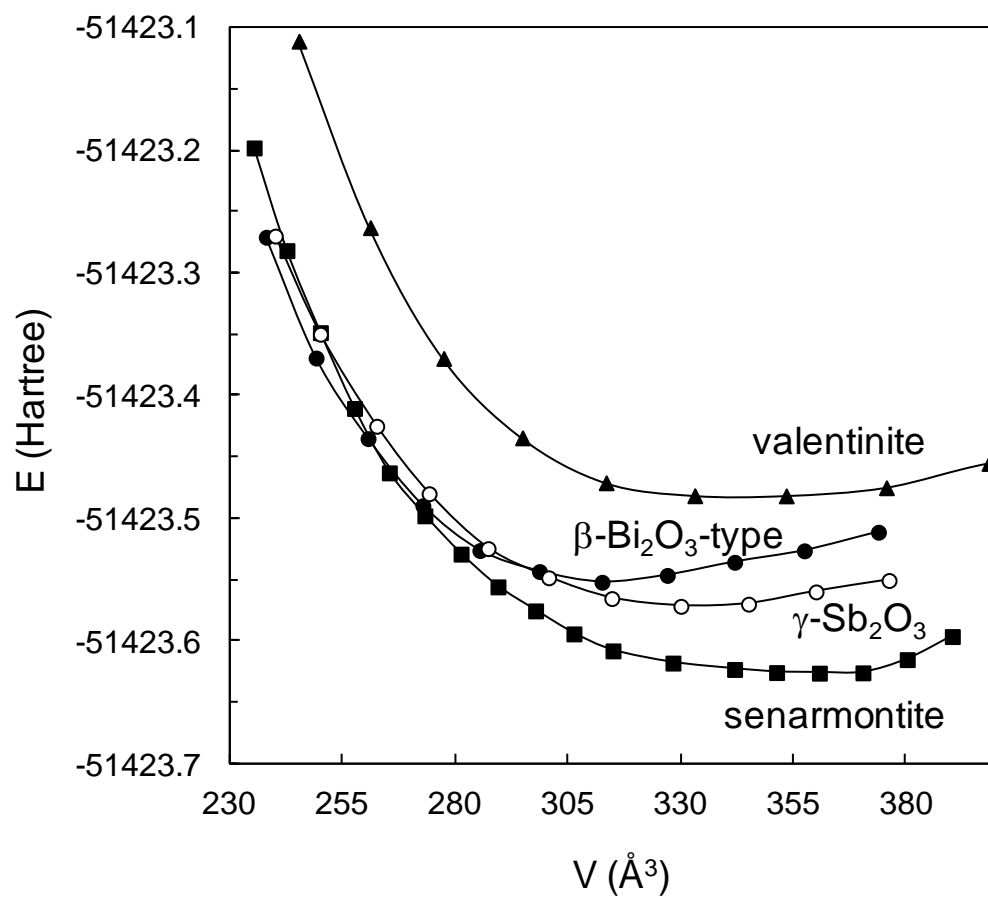


Fig. 10 (a)

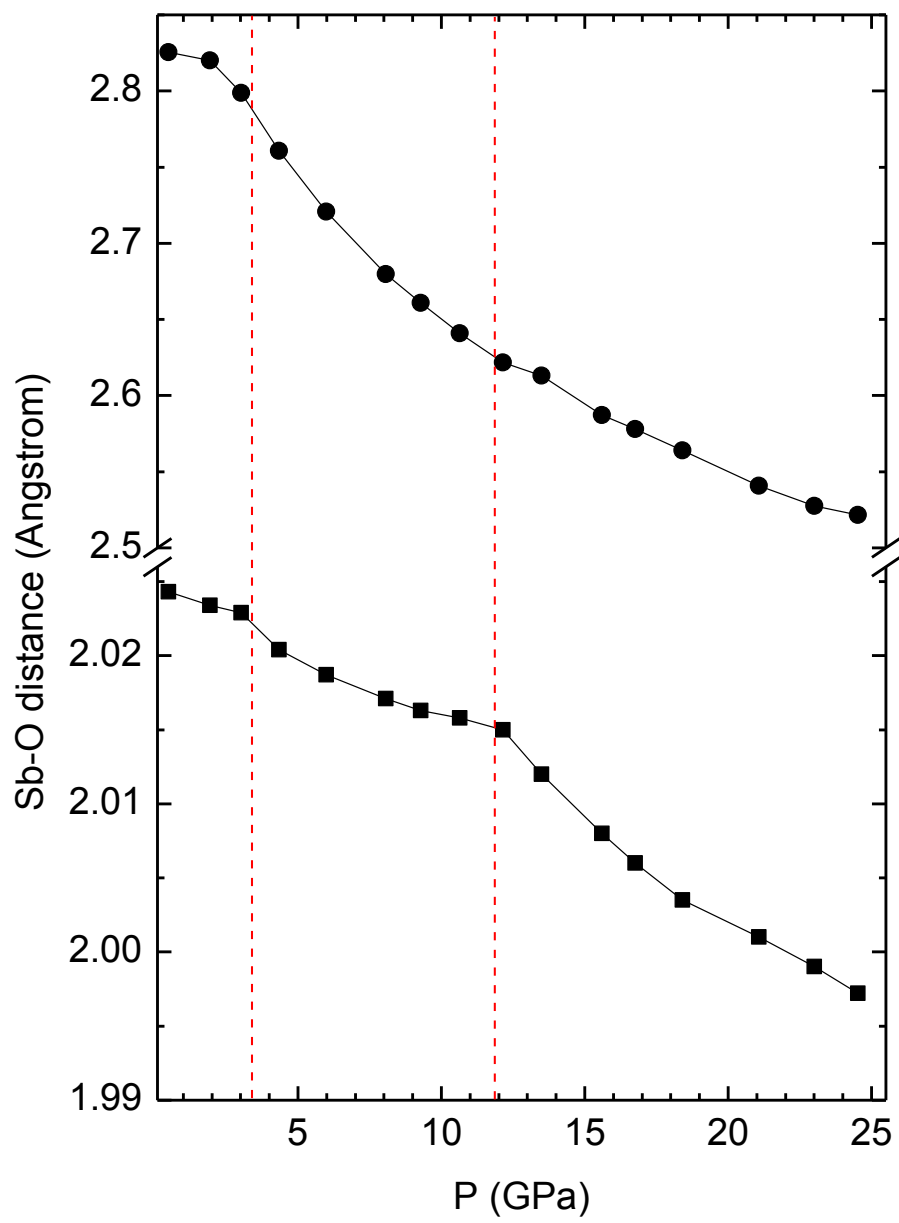
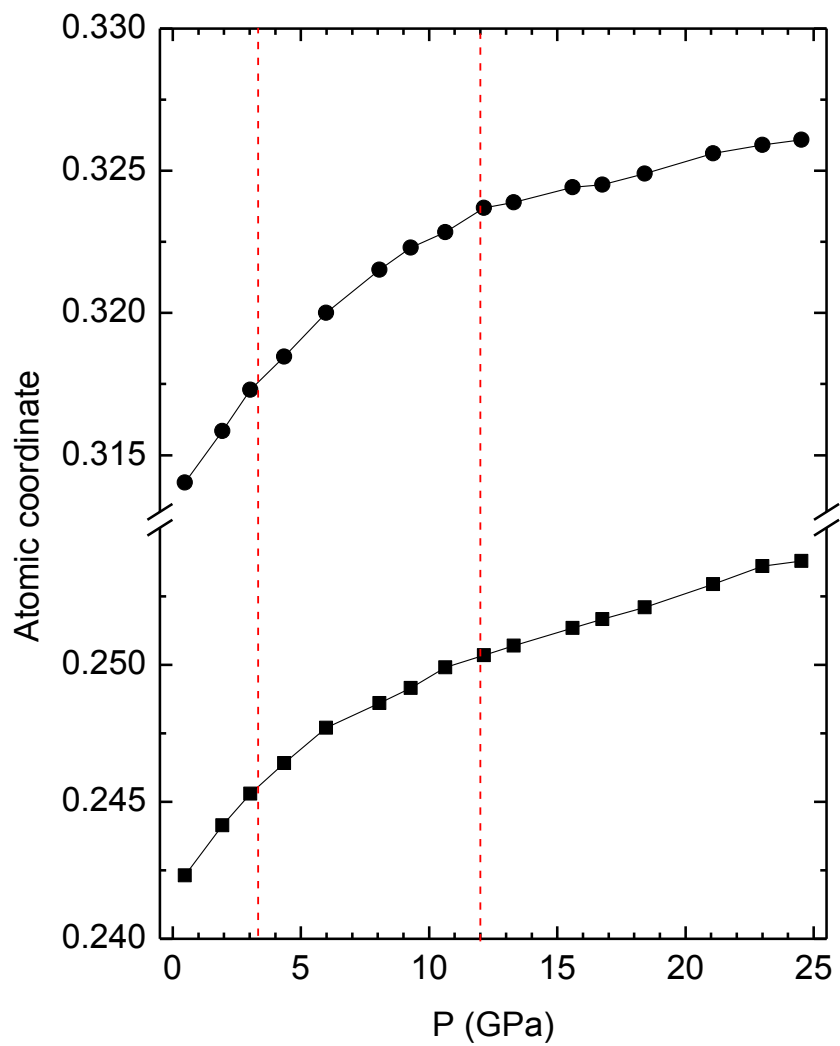


Fig. 10 (b)



**Fig. 11**

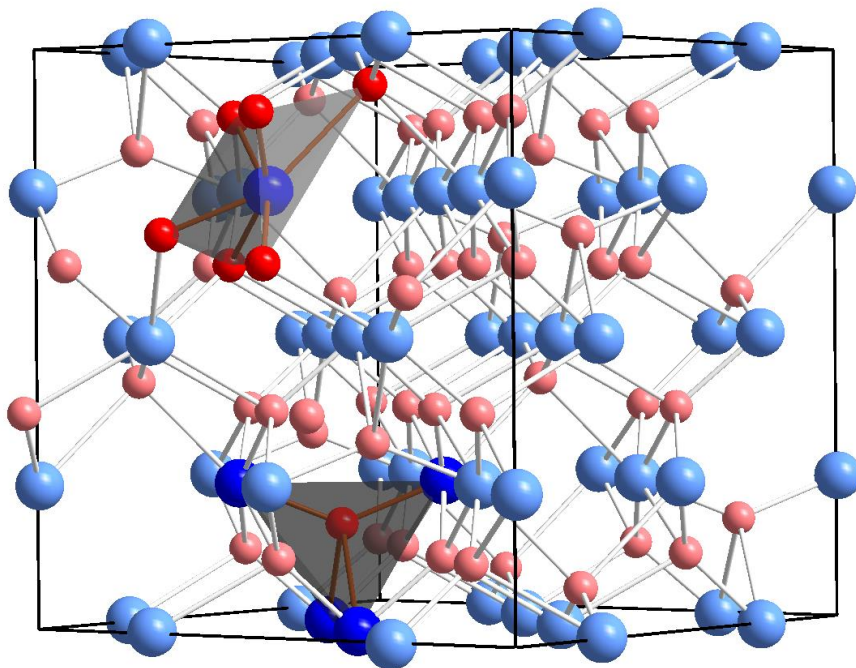
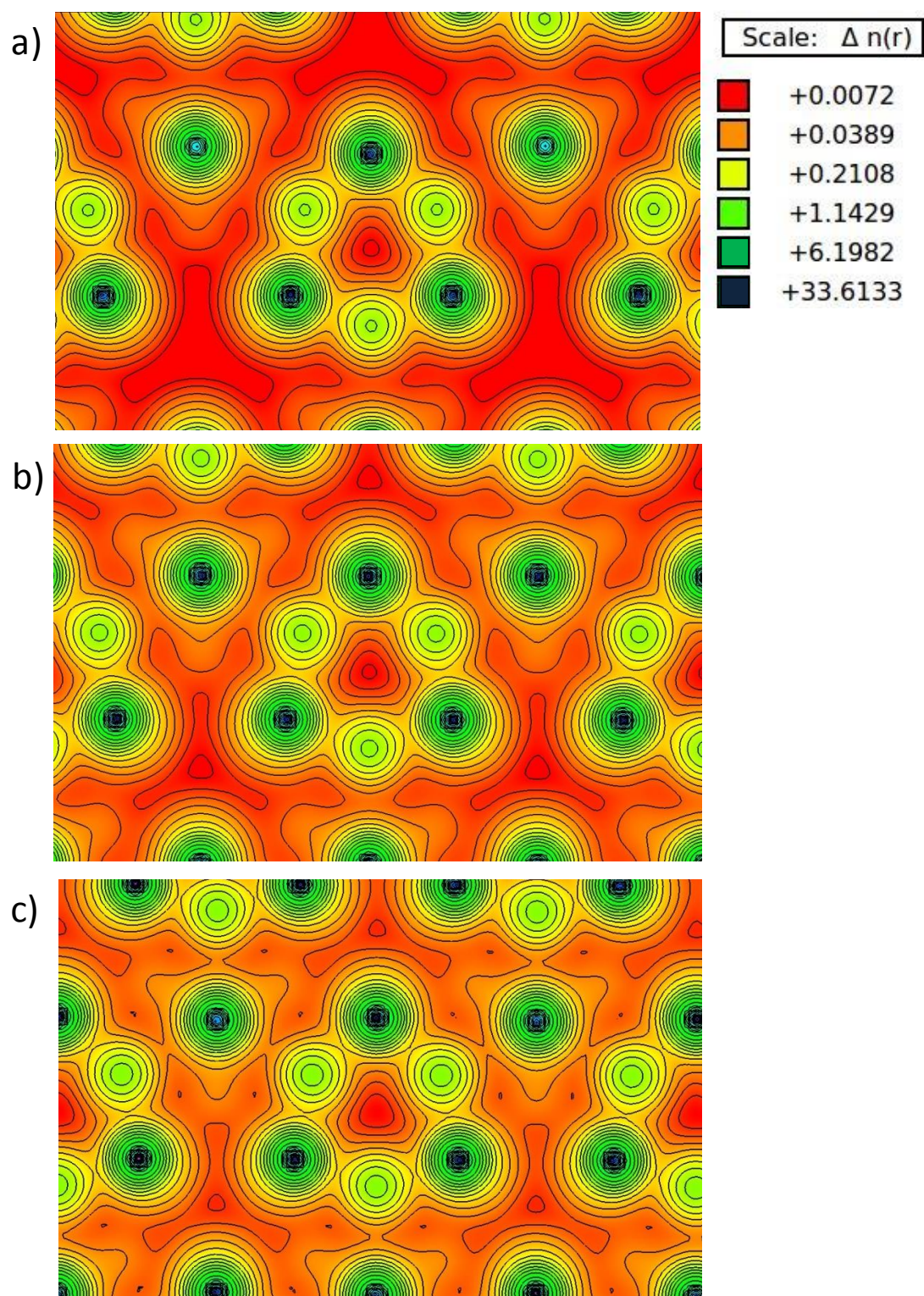
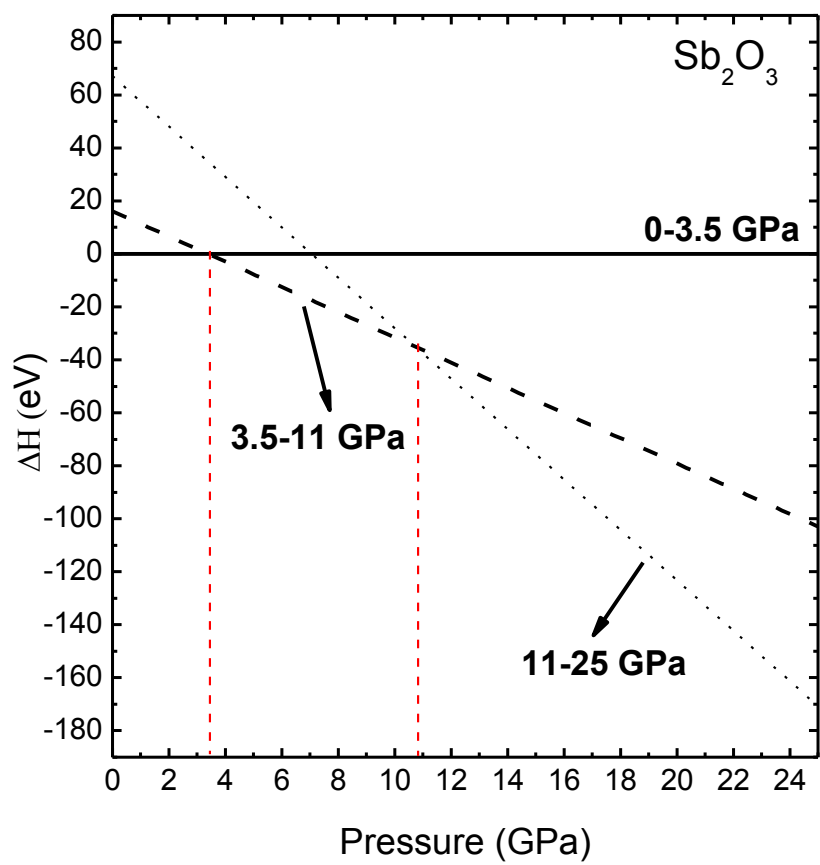


Fig. 12



**Fig. 13**



**Fig. 14**

